Physica Medica 97 (2022) 36–43

Contents lists available at ScienceDirect

Physica Medica

journal homepage: www.elsevier.com/locate/ejmp

Original paper

Composite attenuation correction method using a ^{68}Ge-transmission multi-atlas for quantitative brain PET/MR

João M. Sousa [a,*], Lieuwe Appel [a,b], Mathias Engström [c], Stergios Papadimitriou [d], Dag Nyholm [d,e], Håkan Ahlström [a,b,f], Mark Lubberink [a,g]

[a] Radiology & Molecular Imaging, Department of Surgical Sciences, Uppsala University, Uppsala, Sweden
[b] Medical Imaging Centre, Uppsala University Hospital, Uppsala, Sweden
[c] Collective Minds Radiology AB, Täby, Sweden
[d] Department of Neurology, Uppsala University Hospital, Uppsala, Sweden
[e] Department of Medical Sciences, Neurology, Uppsala University, Uppsala, Sweden
[f] Antaros Medical AB, BioVenture Hub, Mölndal, Sweden
[g] Medical Physics, Uppsala University Hospital, Uppsala, Sweden

ARTICLE INFO

Keywords:
PET/MRI
Hybrid imaging
Attenuation correction
^{68}Ge-transmission scan
[^{11}C]PE2I
Kinetic modelling

ABSTRACT

In positron emission tomography (PET), ^{68}Ge-transmission scanning is considered the gold standard in attenuation correction (AC) though not available in current dual imaging systems. In this experimental study we evaluated a novel AC method for PET/magnetic resonance (MR) imaging which is essentially based on a composite database of multiple ^{68}Ge-transmission maps and T1-weighted (T1w) MR image-pairs (composite transmission, CTR-AC).

This proof-of-concept study used retrospectively a database with 125 pairs of co-registered ^{68}Ge-AC maps and T1w MR images from anatomical normal subjects and a validation dataset comprising dynamic [^{11}C]PE2I PET data from nine patients with Parkinsonism. CTR-AC maps were generated by non-rigid image registration of all database T1w MRI to each subject's T1w, applying the same transformation to every ^{68}Ge-AC map, and averaging the resulting ^{68}Ge-AC maps. [^{11}C]PE2I PET images were reconstructed using CTR-AC and a patient-specific ^{68}Ge-AC map as the reference standard. Standardized uptake values (SUV) and quantitative parameters of kinetic analysis were compared, i.e., relative delivery (R_1) and non-displaceable binding potential (BP_{ND}).

CTR-AC showed high accuracy for whole-brain SUV (mean %bias ± SD: 0.5 ± 3.5%), whole-brain R_1 (−0.1 ± 3.2%), and putamen BP_{ND} (3.7 ± 8.1%). SUV and R_1 precision (SD of %bias) were modest and lowest in the anterior cortex, with an R_1 %bias of −1.1 ± 6.4%).

The prototype CTR-AC is capable of providing accurate MRAC-maps with continuous linear attenuation coefficients though still experimental. The method's accuracy is comparable to the best MRAC methods published so far, both in SUV and as found for ZTE-AC in quantitative parameters of kinetic modelling.

Introduction

Accurate attenuation correction (AC) in positron emission tomography (PET) imaging is a prerequisite for obtaining quantitatively correct images. The transmission scan with rotating ^{68}Ge-rod sources (^{68}Ge-AC) is considered the gold standard for PET AC [1], as it directly obtains linear attenuation coefficient (LAC) values of 511 keV photons. Other methods, like computed tomography (CT)-based AC (CT-AC), require conversion from CT Hounsfield units acquired at lower energy (around 120 keV) to LAC values at 511 keV [2,3]. In a hybrid PET /magnetic

Abbreviations: ^{68}Ge-AC, Germanium-based attenuation correction; AC, Attenuation correction; BP_{ND}, Binding potential (non-displacable); CT, Computer tomography; CTR, Composite transmission; DAT, Dopamine transporter; FOV, Field-of-view; LAC, Linear attenuation coefficient; MRAC, MR attenuation correction; MRI, Magnetic resonance imaging; NEX, Number of excitations; OSEM, Ordered subset expectation maximization; PET, Positron emission tomography; R_1, Relative delivery; SUV, Standardized uptake value; T_1w, T_1 weighted; TAC, Time activity curve; T, Tesla; UTE, Ultrashort echo time; VOI, Volume of interest; ZTE, Zero echo time; 3D, Three-dimensional.

* Corresponding author.
E-mail address: joao.sousa@surgsci.uu.se (J.M. Sousa).

https://doi.org/10.1016/j.ejmp.2022.03.012
Received 23 July 2021; Received in revised form 18 February 2022; Accepted 14 March 2022
Available online 24 March 2022

resonance (PET/MR) system, there is neither a direct nor an indirect way to obtain LAC values, as for stand-alone PET and PET/CT systems, respectively. The main reason is the MR-metal incompatibility which excludes the implementation of a standard rotating rod source, although a non-commercial alternative has been presented for brain PET imaging [4]. Hence, MR compatible AC (MRAC) methods were developed to achieve reliable quantification [2,5–9].

MRAC methods can essentially be separated into three different groups [5,10,11] based on: (1) MR image segmentation, (2) the use of an atlas or database, and (3) emission-based methods, or a combination of any of these with machine learning. Image segmentation uses a classification of MRI data in different tissue types to produce a CT-like image (Pseudo-CT). LAC values are then attributed based either on tissue type or MR intensities. An advantage is that individual structural patient information is considered. The most recent methods, such as ultrashort echo time (UTE) and zero-echo time (ZTE), are also able to take bone into account [12–14]. They provide dependable results, although with a significant bias in absolute radioactivity concentrations compared to ^{68}Ge-AC [15,16] (but not compared to CT-AC [17]). Atlas, database or a combination of these methods, rely on having a database with many subjects to produce a template image that can be converted into the patient space. This approach can be implemented using transmission AC, CT-AC or, images to generate a patient-matched Pseudo-CT along with probabilistic [18–22] or machine learning methods [23–25]. However, patient-specific variations outside the template database, such as skull thickness or bone abnormalities, are not considered. Emission-based MRAC methods are implemented using PET data only, as the AC map is calculated from emission data [26]. The maximum likelihood reconstruction of attenuation and activity (MLAA) method is an example of an iterative reconstruction algorithm that allows the reconstruction of activity distribution alongside the attenuation properties [4]. However, this method does not converge to a single solution and might fail in regions with low radioactivity concentration [27].

For evaluation of MRAC methods, most studies regarded static brain PET using standardized uptake values (SUV) or target-to reference regions in SUV, which solely express the tracer uptake. In a comparative multi-centre study, eleven different MRAC methods were evaluated using a large cohort with static PET/MR data [28]. Generally, the average accuracy of tracer uptake was within acceptable ±5% limits compared to CT-AC. The last few years, an increasing number of studies [19,21,23,29,30] reported MRAC assessments from dynamic brain PET data acquisitions allowing derivation of quantitative kinetic parameters, illustrating physiological processes over time. Although most studies show an acceptable accuracy, direct comparisons of the results are impeded due to differences in methodology, especially choice of radiotracer and kinetic modelling approach. Further, CT-AC was considered as reference standard which may cause an additional bias compared to the use of a ^{68}Ge-based AC [3].

In this work, we evaluated an in-house developed composite AC method for PET/MR imaging based on a composite database comprising ^{68}Ge-transmission maps and T1-weighted (T1w) MR image-pairs from many subjects. This multi-atlas approach, called CTR-AC (CTR, composite transmission), provides a ^{68}Ge-based AC with continuous LAC values to any subject scanned on a PET/MR system. Our hypothesis is that CTR-AC map will result in a more accurate representation of photon attenuation compared to CT- and MR-based AC methods. This work is built on previous studies where we compared Atlas-, ZTE-, and MaxProb-MRAC (multi-atlas approach using maximum probability) to the gold standard ^{68}Ge-AC using both static and dynamic brain PET images of the dopamine transporter (DAT) ligand [^{11}C]PE2I [15,16]. ZTE- and MaxProb-MRAC demonstrated similar accuracy, but ZTE-MRAC demonstrated consistently a higher precision in SUV and quantitative kinetic parameters, compared to ^{68}Ge-AC. As the field-of-view (FOV) of the stand-alone PET scanner was about 40% smaller compared to the PET-MR scanner, we needed individual MRAC images for resampling and completion of neck information. In the current study, we used individual ZTE-MRAC images as it was the best method available on our PET/MR system.

Hitherto, no study has evaluated a multi-atlas approach using ^{68}Ge-transmission maps in dynamic PET data on the quantitative outcome parameters using kinetic modelling applications. Yet, there is one other research group which reported a similar approach obtaining template-based attenuation maps using MR and ^{68}Ge-transmission scans for reconstruction of PET data acquired on a PET/MR system [22,31]. However, their template was grounded on a small number of subjects and the validation was done in static [^{18}F]FDG brain images. Further they evaluated regional SUVs and were using CT-AC as reference method [31].

The aims of this proof-of-concept study were two-fold: (1) generation of a reliable CTR-AC map; (2) evaluation of the CTR-AC method in a clinical validation dataset, using in both cases ^{68}Ge-AC as the gold standard. In the first part, we evaluated the absolute differences between CTR- and ^{68}Ge AC maps, both for tissue classes and voxel-wise over the whole-brain. In the second part, we used the same dynamic [^{11}C]PE2I PET/MR data as in our previous studies [15,16] for validation of CTR-AC, allowing even comparisons to former results. Evaluation criteria were accuracy and precision, using ^{68}Ge-AC as golden standard, for SUV as well as binding potential and relative delivery obtained from a kinetic modelling approach. The evaluation was completed with voxel-wise brain analyses for all quantitative outcome parameters.

Methods

^{68}Ge-AC and MRI database

Data were selected retrospectively from our research database and comprised 125 pairs with a ^{68}Ge-AC map and a 3D T1w MR image. For details, see supplemental data (S1). The included T1w MR images in our database should be anatomical normal. Furthermore, the MR images should have a good quality showing a high soft tissue contrast, well defined borders, and absence of artefacts. Each ^{68}Ge-AC map was based on a 10 min transmission scan with rotating ^{68}Ge-rod sources acquired on an ECAT Exact HR+ stand-alone PET device (Siemens/CTI PET Systems Inc, Knoxville, TN, USA) prior to injection of radioactivity. The transmission scans were reconstructed using ordered subset expectation maximization (OSEM) with 6 iterations, 8 subsets, and a 4 mm Hanning post-filter. All ^{68}Ge-AC maps had the same matrix size and voxel size as in the validation dataset: 128 × 128 × 63 voxels and 5.15 × 5.15 × 2.43 mm^3, respectively. Most of the T1w MR images (> 85%) were acquired on a 3 T MRI system (Achieva, Philips Healthcare, Cleveland), with the remainder being acquired on other 1.5 T and 3 T MRI scanners (n = 18).

Validation dataset

We used retrospectively the same imaging data as in our previous studies [15,16]. Shortly, nine patients with Parkinsonism (5 female; age range 49–82 years) underwent an 80 min dynamic PET scan consisting of 22 frames with increasing duration (4 × 60 s, 2 × 120 s, 4 × 180 s, 12 × 300 s) after injection of 5 MBq/kg body weight [^{11}C]PE2I on a 3 T, time of flight PET/MR scanner (SIGNA PET/MR, GE Healthcare, Waukesha, WI, USA). Simultaneously, two scans related to this study were acquired: (1) a ZTE sequence [13,14] (duration 153 s, 4 NEX, FOV 260 mm, slice thickness 1.4 mm, no slice gap, matrix 192 × 192, flip angle 0.8°) and (2) a 3D T1w brain volume sequence (gradient-echo, duration 272 s, 1 NEX, FOV 250 mm, slice thickness 1 mm, matrix 256 × 256, flip angle 12°, TI 450 ms). All patients had a previous investigation on a stand-alone PET scanner including acquisition of ^{68}Ge-AC transmission data (within 6 months). The acquisition and reconstruction protocol used were the same as described for the database. None of the patients showed severe brain atrophy.

Generation of a composite ^{68}Ge-transmission AC map

Fig. 1 illustrates the generation of a composite ^{68}Ge-transmission AC map (CTR-AC). For every pair of images in the database, the T1w MR image was co-registered to the corresponding ^{68}Ge-AC image using the FSL affine registration tool FLIRT [32,33]. Then, all T1w MR images in the database were spatially normalised to each subject's T1w image (FSL FNIRT; for details, see supplemental data (S2)). The resulting transformation matrices were then applied to corresponding ^{68}Ge-AC maps, and a CTR-AC map was generated voxel-wise as the mean of all registered ^{68}Ge-AC maps. Zero voxel values in any of the registered ^{68}Ge-AC maps were ignored when calculating the voxel mean. The average CTR-AC map was resampled to a MRAC matrix size of 128 × 128 × 89 voxels with dimensions 4.68 × 4.68 × 2.78 mm. Individual ZTE-MRAC data was used to complete missing neck information for each patient in the validation dataset due to the differences in axial FOV between the standalone PET and PET/MR scanners, 155 and 300 mm, respectively. ZTE-MRAC was chosen because we have shown it is the most correct AC method available to us [16]. Finally, the CTR-AC map was completed with head coils and bed information supplied by the PET/MR manufacturer.

Generation of ^{68}Ge-AC map for PET/MR

The computation of the patients' ^{68}Ge-AC map for PET/MR was previously described [15]. The ^{68}Ge-transmission map was co-registered to the ZTE-MRAC map. In four patients, the top of the skull was missing, and these images were completed using ZTE-MRAC data. Like CTR-AC, head coils and bed information were added.

Image reconstruction

The [^{11}C]PE2I PET data were reconstructed with both CTR- and ^{68}Ge-AC methods, using time-of-flight ordered subset expectation maximization with 2 iterations, 28 subsets, a 300 mm FOV, a 5 mm Gaussian post-filter, and reconstruction matrix of 192x192x89 voxels. All appropriate corrections for quantitative image reconstruction were applied as included in the PET/MR software.

Data evaluation

Patients' motion during scanning was estimated from the ^{68}Ge-AC-based [^{11}C]PE2I PET images on a frame-by-frame basis, where each time point was realigned to the previous starting with a 0–3 min reference image. The same motion correction was applied to both datasets. For all patients, the T1w MR images were co-registered to the 0–3 min reference image and segmented into grey matter, white matter, and cerebral spinal fluid using SPM 12 [34]. Thereafter, a probabilistic volume of interest (VOI) template was applied using PVElab [35]. Time activity curves (TACs) were acquired by projecting the grey matter VOIs over the dynamic [^{11}C]PE2I PET datasets, and regional SUVs were obtained by normalization of the activity values by patient weight and injected radioactivity dose. Parametric [^{11}C]PE2I R_1 (relative delivery, reflecting cerebral blood flow relative to cerebellum) and BP_{ND} (non-displaceable binding potential, proportional to DAT availability) images were derived using a basis function implementation of the simplified reference tissue model [36,37] with the cerebellar grey matter as a reference region. The same VOI template was projected on the parametric images to obtain regional R_1 and BP_{ND} estimates.

VOIs were grouped in clusters of regions for assessment of SUV and R_1. The brain clusters comprised anterior cortical regions (ACR; frontal gyrus, dorsolateral and ventrolateral prefrontal cortexes), posterior cortical regions (PCR; occipital cortex, parietal cortex), dorsal striatal regions (STR; caudate nucleus, putamen), limbic regions (LR; amygdala, hippocampus, hypothalamus, and thalamus), whole-brain (WB; grey matter) and cerebellum. For evaluation of BP_{ND} quantification, only areas with high DAT density were considered: caudate nucleus and putamen.

To compare LAC values for both methods, grey matter and bone VOIs were created on the respective AC maps. A grey matter VOI was created as a sphere containing a large portion of brain tissue. Threshold segmentation followed by two pixel erosion of the AC map was used to calculate the bone VOI, as previously described by Sousa et al. [15].

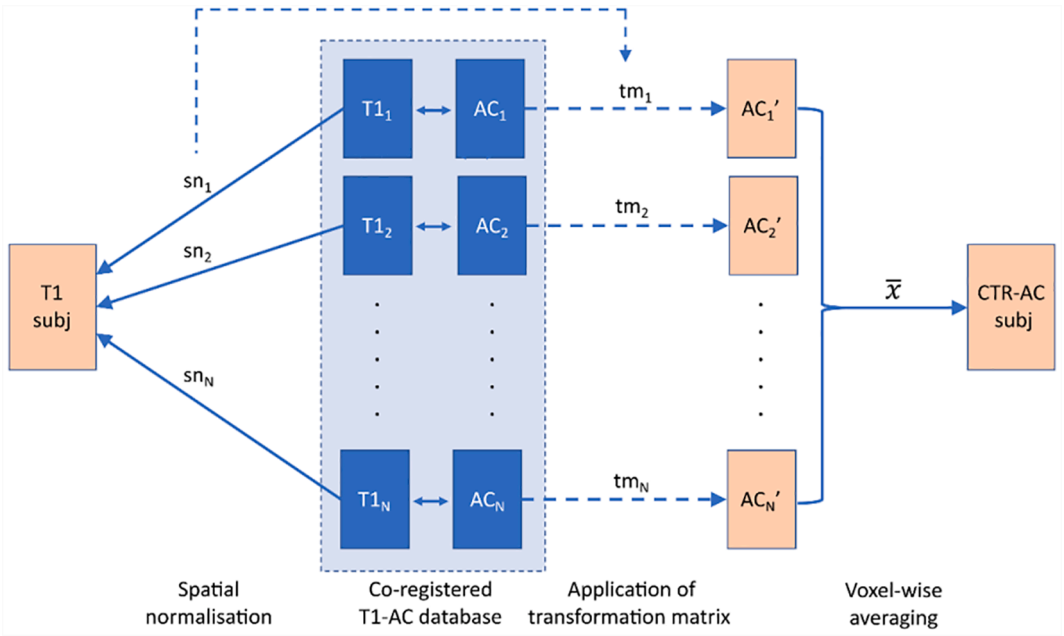

Fig. 1. Generation of a composite ^{68}Ge-transmission AC map (CTR-AC) using a database of co-registered T1-MR images ($T1_1$ to $T1_N$) and ^{68}Ge-AC maps (AC_1 to AC_N). All database T1 images were spatially normalised to a subject's individual T1 image (sn_1 to sn_N). The resulting transformation matrices (tm_1 to tm_N) were applied to the corresponding database ^{68}Ge-AC images. The subject's CTR-AC map was then calculated by voxel-wise averaging of the generated AC maps (AC_1' to AC_N'). Blue: database space; orange: subject space.

Statistical analysis

For VOI-based analyses, accuracy was defined as the relative difference (%bias) between CTR-AC and ^{68}Ge-AC (Eq. 1), and precision as the standard deviation of the %bias:

$$Bias(\%) = \frac{PET_{CTR-AC} - PET_{68Ge-AC}}{PET_{68Ge-AC}} \times 100 \quad (1)$$

with *PET* referring to either SUV, R_1 or, BP_{ND}.

For voxel-wise analyses, SUV and parametric images (R_1 and BP_{ND}) were spatially normalized to a common image space (MNI) using SPM12. Then, absolute differences (bias) were calculated at the voxel level according to Eq. 2:

$$Bias = PET_{CTR-AC} - PET_{68Ge-AC} \quad (2)$$

Hence, mean images (SUV, R_1 and BP_{ND}) based on all patients were calculated for CTR-AC, ^{68}Ge-AC and absolute bias.

Correlation rank-order analysis (Spearman) and orthogonal regression analysis were calculated to assess degree of agreement between CTR-AC and ^{68}Ge-AC for R_1 and BP_{ND}. Significant differences (p-value $<$ 0.05) between CTR- and ^{68}Ge-AC were evaluated using a Wilcoxon matched-paired signed-rank test. All statistical analyses were conducted in GraphPad Prism 8 (GraphPad Software Inc, La Jolla, CA, USA).

Results

Data from one female patient was excluded. In this case the method providing a ZTE neck completion failed, which resulted in an incorrect AC map at the neck region.

CTR-AC and ^{68}Ge-AC attenuation maps are presented for a representative patient in Fig. 2, along with the absolute differences between maps. In this subject, the ^{68}Ge-AC required completion in the skulĺs superior section, as seen in Fig. 2b, creating a slightly increased negative absolute bias in that area (Fig. 2c). In brain tissue classes, CTR-AC showed a relative bias of 0.9% ± 5.5% in soft tissue, and in bone, 2.1% ± 2.4% in terms of LAC values.

Mean 80 min [^{11}C]PE2I SUV images based on CTR-AC and ^{68}Ge-AC, and the corresponding absolute bias, are presented in Fig. 3. Differences are hard to detect by visual inspection. However, the bias image demonstrated a slight positive bias in central and anterior sections, especially at the level of the striatum. In contrast, a minor negative bias was observed in posterior areas. All differences were in the range of −0.05 and 0.07 SUV units.

Mean CTR-AC and ^{68}Ge-AC TACs were similar for all brain clusters

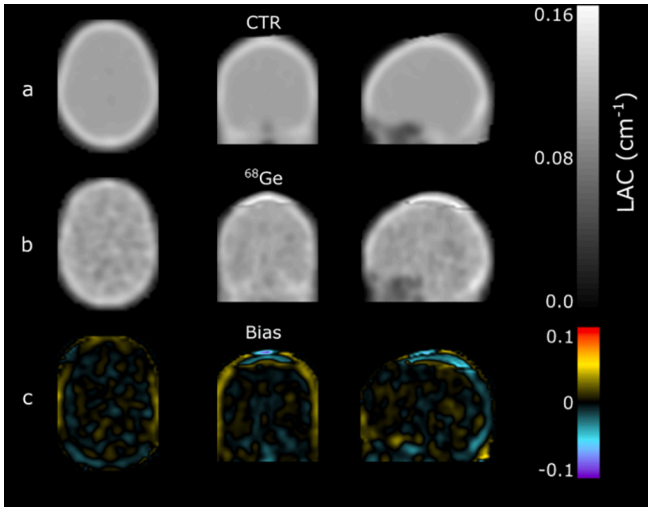

Fig. 2. AC maps for a representative patient: (a) CTR-AC, (b) ^{68}Ge-AC, and (c) corresponding absolute bias.

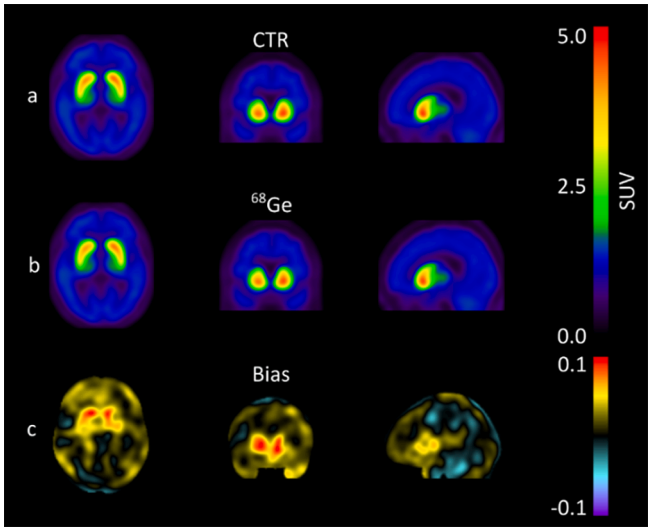

Fig. 3. Mean SUV images (n = 8) for (a) CTR-AC, (b) ^{68}Ge-AC, and (c) corresponding absolute bias.

(Fig. 4a) and the mean bias of CTR-AC relative to ^{68}Ge-AC was at any time below 2% for all clusters (Fig. 4b). Time-variability was found for the cerebellum with a slightly increasing negative bias and increased interpatient variability towards the end of the scan. For the other brain clusters, the bias and interpatient variability were almost constant over time.

Mean parametric [^{11}C]PE2I R_1 images for CTR-AC and ^{68}Ge-AC are presented in Fig. 5a and b. The difference image (Fig. 5c) illustrates a marginal overestimation in the frontal and medial regions, and underestimation in the brain's posterior section of the brain.

Relative bias and relationships between CTR- and ^{68}Ge-AC based R_1 values are presented at VOI levels in Fig. 6 and Table 1. No significant bias was found. The mean relative bias was close to zero, with cortical regions showing a slightly negative bias and the subcortical regions a slightly positive non-significant bias. Cortical brain clusters (ACR, PCR) showed considerably higher variability than subcortical clusters (STR, LR), but overall, the variability was about 3% (WB). Consequently, correlations (r) in cortical areas were around 0.9, whereas the correlations for subcortical regions were close to one. The regression slope was only significantly different from identity for anterior cortical regions.

Mean parametric [^{11}C]PE2I BP_{ND} images for CTR-AC and ^{68}Ge-AC based PET images were visually equivalent, but a minor positive absolute bias was observed across the brain, above all at the level of the striatum (Fig. 7).

For striatal regions, a bias of about 3.5% was found, although there was a substantial interpatient variability (Fig. 8 and Table 2). The slopes of the orthogonal regression lines between CTR-AC and ^{68}Ge-AC were not significantly different from identity, and the corresponding correlations were close to one.

Discussion

In this proof-of-concept study, we presented a new ^{68}Ge-transmission multi-atlas AC method to be used for AC of brain PET data in PET/MR systems, using a database of pairs of ^{68}Ge-AC and T1w MR images. The CTR-AC map showed a small bias in brain tissue classes and voxel-wise in the whole-brain compared to the gold standard for measurement of linear attenuation coefficients for 511 keV photons, the ^{68}Ge-transmission scan. This method was validated using dynamic [^{11}C]PE2I scans, showing overall a high accuracy and a modest precision against ^{68}Ge-AC. To our knowledge, three other studies [19,21,23] have assessed the impact of a kind of composite MRAC map on the outcome parameters of kinetic modelling. In these studies, accuracy was high (%

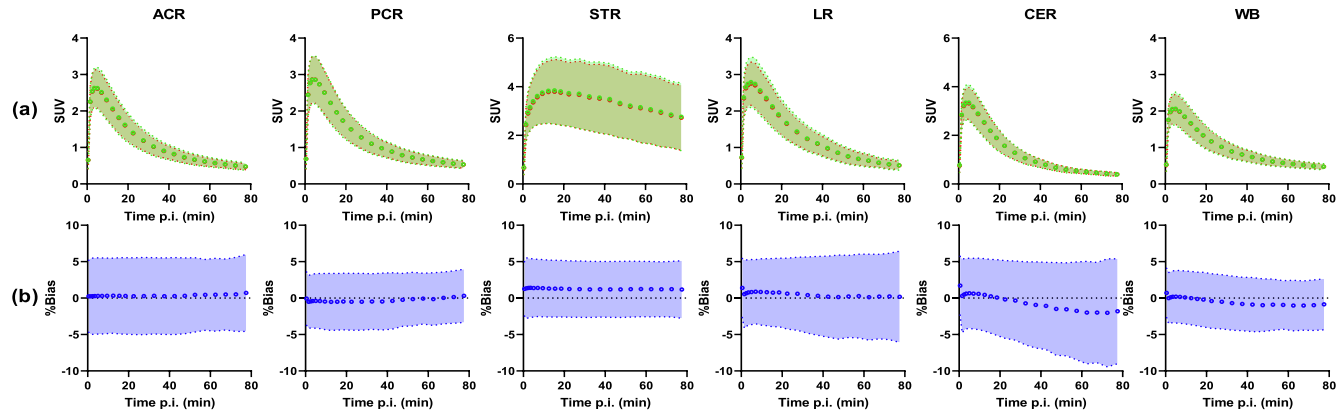

Fig. 4. Mean SUV over time (a) and (b) relative bias over time for different brain clusters. The green points represent CTR-AC SUV values and the red points ^{68}Ge-AC. ACR anterior cortical regions, PCR posterior cortical regions, STR striatal regions, LR limbic regions, CER cerebellum, and WB whole-brain grey matter. The solid points represent mean values, while shaded areas show standard deviation.

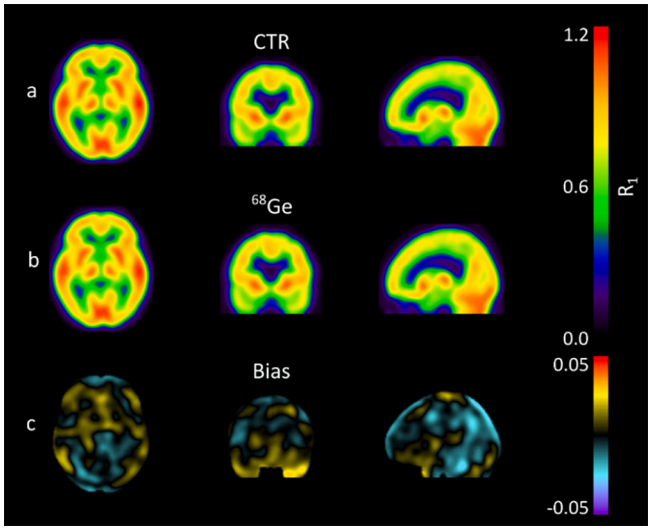

Fig. 5. Mean parametric R_1 images (n = 8) when using (a) CTR-AC, (b) ^{68}Ge-AC, and (c) corresponding absolute bias.

bias < ±5%) compared to CT-AC, but as mentioned before the used radiotracers have different kinetic properties which make an in deep comparison difficult. On a longer term, the present work could contribute to development of an accurate ^{68}Ge-based AC with continuous LAC values for quantitative neuro PET/MR.

The mean bias in SUV values was close to zero (Fig. 4), with a standard deviation of approximately 3–5%. Compared to the multicentre study of MRAC methods by Ladefoged and colleagues [28], CTR-AC accuracy would rank among the best three methods while precision was slightly worse than the best-ranking methods. One must

Table 1
R_1 Mean accuracy (%bias), precision (SD of %bias), and Spearman correlation coefficient (r) for all brain clusters. Additionally, slope and intercept of orthogonal regression lines are given.

VOI Cluster	%Bias	SD (%)	r	Slope	Intercept
WB	−0.10	3.17	0.90	1.12	−0.10
ACR	−0.56	6.38	0.91	1.22*	−0.17
PCR	−1.09	5.39	0.87	1.10	−0.09
STR	0.70	3.41	0.97	0.99	0.01
LR	0.08	2.17	0.98	1.03	−0.02

ACR anterior cortical regions, PCR posterior cortical regions, STR striatal regions, LR limbic regions, WB whole brain grey matter. * p-value < 0.05, Wilcoxon matched-paired signed rank test.

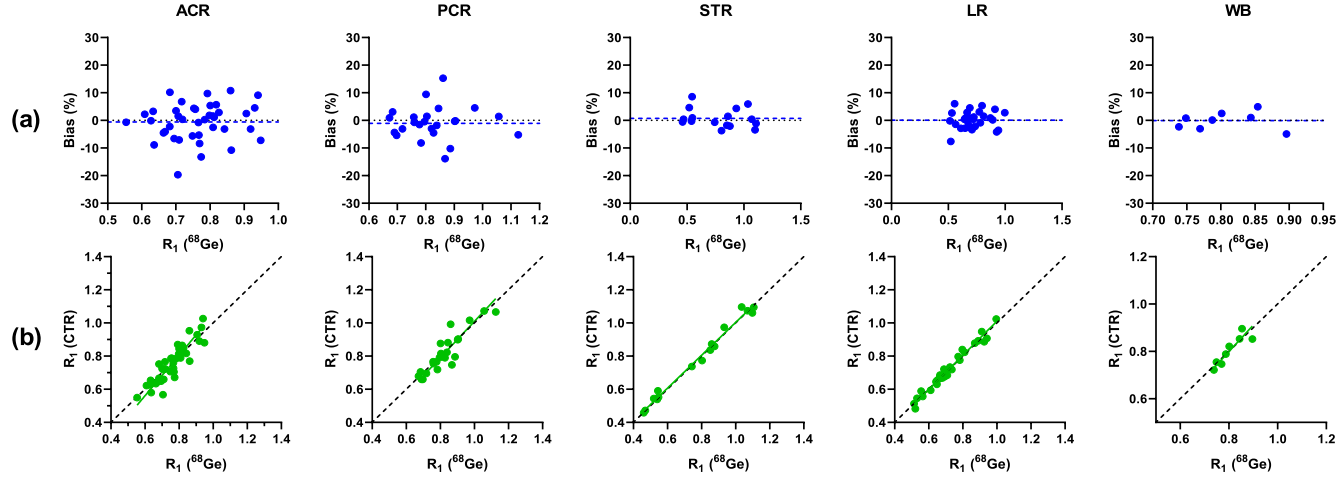

Fig. 6. Relative delivery (R_1) - (a) %bias (and (b) relation between CTR- and ^{68}Ge-AC based values for the various brain clusters. ACR anterior cortical regions, PCR posterior cortical regions, STR striatal regions, LR limbic regions, CER cerebellum, and WB whole-brain grey matter. The solid line is the orthogonal regression fit, and the dashed line is the line of identity.

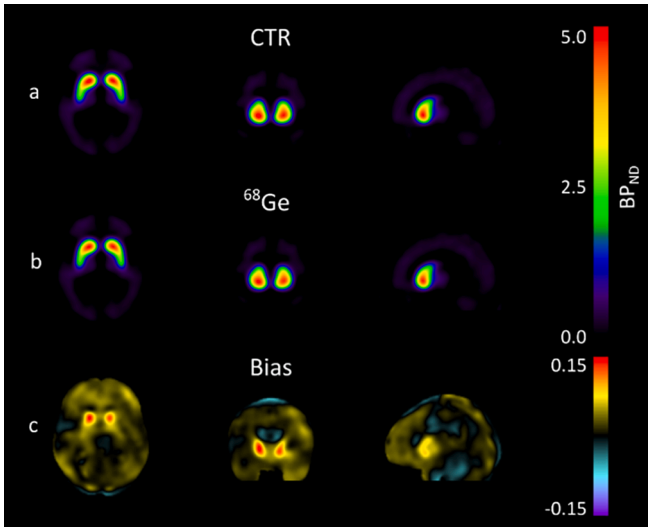

Fig. 7. Mean parametric BP_{ND} images (n = 8) when using (a) CTR-AC, (b) ^{68}Ge-AC, and corresponding (c) absolute bias.

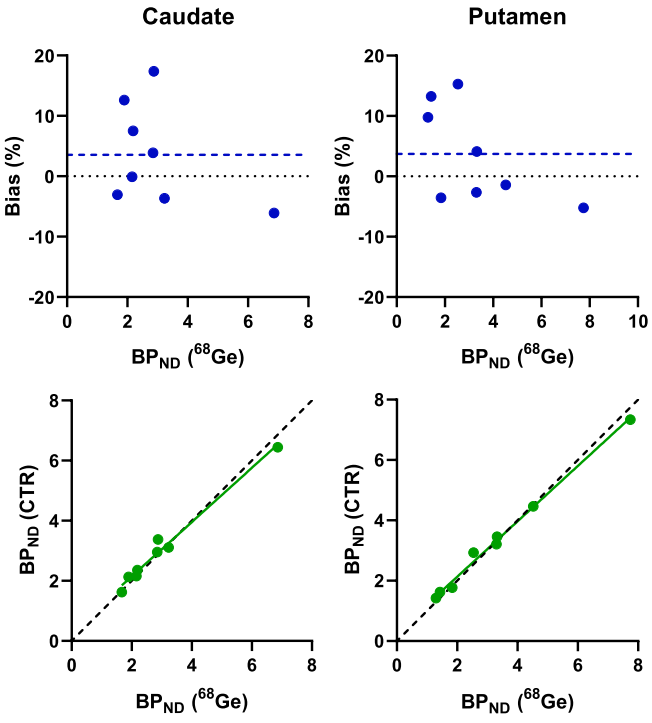

Fig. 8. Binding potential (BP_{ND}) – (a) %bias and (b) relation between CTR- and ^{68}Ge-AC based values for caudate and putamen. The solid line is the regression fit, and the dashed line is the line of identity.

Table 2
BP_{ND} – Mean accuracy (%bias), precision (SD of %bias), and Spearman correlation coefficient (r) for all brain clusters. Additionally, slope and intercept of orthogonal regression lines are given.

VOI	%Bias	SD (%)	r	Slope	Intercept
Caudate	3.56	8.37	0.98	0.90	0.34
Putamen	3.70	8.11	1.00	0.92	0.30

*p-value < 0.05, Wilcoxon matched-paired signed rank test.

keep in mind that they used [^{18}F]FDG, whereas we used [^{11}C]PE2I. However, the initial frames of a dynamic [^{11}C]PE2I scan essentially show cerebral blood flow, which has a similar distribution as [^{18}F]FDG [38]. When only looking at the first four minutes of the [^{11}C]PE2I scan the CTR-AC shows a bias of 0.5 ± 3.4% in SUV, which can be compared to the results by Ladefoged *et al.* [28] and emphasised the relatively high accuracy of CTR-AC. We previously compared ZTE-MRAC to ^{68}Ge-AC [16] and found for WB an average moderate SUV bias of about 8% together with a very high precision (1.5%). The substantial bias of ZTE-MRAC compared to the methods investigated by Ladefoged *et al.* [28] might also be due to the use of different reference methods, ^{68}Ge-AC and CT-AC, respectively. Rota-Kops *et al.* [22,31] evaluated template-based ^{68}Ge-AC against CT-AC investigating accuracy of regional SUVs of static [^{18}F]FDG images in eleven subjects acquired on a hybrid 3 T MR-BrainPET scanner (Siemens Medical Solutions Inc, Knoxville, TN, USA). Despite observed differences in classifications of bone and soft tissue between both methods, they found a high accuracy and precision for template-based ^{68}Ge-AC (relative bias < ±4%; SD at most 2.5%). Sekine *et al.* [17] compared ZTE-MRAC to CT-AC, and they also found a bias close to zero. In summary, in terms of SUV, CTR-AC shows high accuracy and moderate precision.

As for SUV, we found high accuracy and moderate precision in the quantitative parameters R_1 and BP_{ND} after reconstruction with CTR-AC. For R_1, the average %bias varied between −1.1 and 0.7% resulting in an accuracy which was comparable to or higher than previously found for ZTE-MRAC (-0.5–3.3%) [16]. R_1 precision was equivalent in subcortical areas (2.0–3.5%) but substantially lower than ZTE-MRAC in cortical regions (1.5–2.5%). For striatal regions, CTR-AC showed a lower accuracy for BP_{ND} compared to ZTE-MRAC (−0.8–1.8%), but still within acceptable limits of ± 5%. BP_{ND} precision was comparable in caudate (7.4%) and lower in putamen (3.8%), as previously found for ZTE-MRAC and should be considered as moderate (5–10%).

CTR-AC LACs show a non-significant difference of 0.9 ± 5.5% and 2.1 ± 2.4% in soft tissue and bone, respectively, compared to the individual patients' ^{68}Ge-AC maps. Differences between tissue types in our study are comparable to those reported when using more complex deep learning transmission maps [23]. Further, the CTR-AC maps have a much smaller bias than the vendor-provided AC, single atlas [18], and ZTE [13,14,39], where differences are around 3% in soft tissue and from 4 to 18% in bone were found. This modest bias is mainly caused by a LAC for soft tissue of 0.100 cm^{-1} in most MR-based methods versus measured values of around 0.097 cm^{-1} in ^{68}Ge-AC images [15].

In recent years several machine learning techniques, using deep learning with convolutional neural networks, have been proposed for MR-image segmentation. The resulting pseudo-CT can be used for brain PET AC on a PET/MR system [24,25,40,41]. All mentioned studies showed promising results with a high accuracy, but the clinical evaluations were mostly restricted to static [^{18}F]FDG PET images. An exception was the study by Spuhler *et al.* [23] who evaluated a pseudo-CT map based on T1w MRI data compared to a ^{68}Ge-AC map in static and dynamic data of PET scans for two different serotonin tracers, [^{11}C]WAY-100635 and [^{11}C]DASB. For the pseudo-CT the mean relative bias was −1.1 ± 0.8% which is in line with our results. In general, the mean relative bias was < 3% in static and dynamic outcome parameters, where the latter were derived using a kinetic modelling approach. However, although these results are encouraging, they cannot be directly compared to our results due to different tracer properties. Furthermore, in contrast to our study, no direct validation was conducted on a PET/MR system.

Additional factors could have contributed to the differences between the CTR-AC and the reference AC method. Atlas-based methods used to have an outstanding performance. Nevertheless, in practice, patient variations and algorithm limitations exist, which will not allow for a perfect co-registration between the atlas and patient data. Outliers with abnormal morphologies will affect the co-registration, and thereby decrease the performance of the atlas-based AC map [19,20].

Furthermore, a more robust validation of CTR-AC, would be by comparison to a ^{68}Ge-AC map acquired directly in the PET/MR as suggested by Renner *et al.*[4], and thereby evading any negative co-registration issues. However, such a comparison is technically challenging and cannot be done using commercially available technology.

The presented CTR-AC methodology has benefits and limitations, which need to be addressed. Based on multiple ^{68}Ge-transmission maps this MRAC method has the advantage of providing continuous LAC values. Although, the averaging approach might reduce the range of LAC values compared to a standard ^{68}Ge-AC maps, this approach still allows for more correct LAC values at the interface region between tissues compared to discrete tissue-class methods. In our case there is no need for tissue segmentation which avoids possible misclassification errors. Further the CTR-AC approach is a relatively simple and straightforward approach compared to most other published methods, especially pseudo-CT AC along with machine learning methods using convolutional deep neural networks. Deep learning models demand big data for training and testing in patients and healthy volunteers. Further a long process is often required to train the neural network for producing a reliable pseudo-CT. On the other hand, the presented CTR-AC map can be implemented directly in all subjects regardless their health status. Beside the database with pairs of ^{68}Ge-transmission and structural MRI data, no big data is needed. Consequently, the validation of this method could be based on relative few subjects.

The CTR-AC method provides excellent accuracy, but precision slightly lower as shown with other MRAC methods. One possible reason for this may be related to inaccuracies induced by co-registration of the database images to the individual patient images. The 15.5 cm FOV of our ECAT system means that most database images are truncated immediately below the cerebellum and that parts of the top of the skull often were missing, which may cause inaccuracies in the resulting CTR-AC images. The lack of information in the top of the skull can be easily derived from ^{68}Ge-transmission images in the database which contain entire skull information. However, neck information is absent in all ^{68}Ge-transmission images. This absence of information makes the CTR-AC method dependent on an additional MRAC map for completion of the missing information. A possible solution to this problem could be achieved by artificially reconstructing the patient neck section using the T1w image as template. In fact, other MRAC maps native to each scanner can be used, for example, previously we used Atlas-MRAC for this purpose [15,16]. Ideally, the CTR-AC database should be based on ^{68}Ge-transmission images from a stand-alone PET scanner with the same FOV as the SIGNA PET/MR to avoid the need for completion of the skull and neck. To our knowledge the only such scanner is the ECAT HRRT [42] but this scanner uses a ^{137}Cs point source for transmission scanning resulting in an energy of 662 keV which requires conversion to 511 keV attenuation values as well. However, despite this FOV-related limitation, the current approach already showed a high accuracy and provides a solid ground for further studies and refinement of the CTR-AC method.

Our database included pairs of T1w MR and ^{68}Ge-AC images of 125 anatomically normal subjects, which was the total number of image pairs with a good quality T1w MRI and reconstructed ECAT ^{68}Ge-transmission images that were readily accessible from our archive. We feel confident about the size of the database. Though a smaller number of database pairs might have been sufficient, optimisation of the number of included image pairs to speed up the method will be subject of future work. This novel approach was tested in a small group of patients with normal anatomy, however extending the number of patients was not possible, as the stand-alone PET scanners were no longer available. This method is still experimental and time-intensive, and as such it is not ready for routine application, but the obtained results are promising. Hence, CTR-AC should be evaluated in a larger patient cohort and compared to the best available MRAC method. It is also important to include patients with irregular skull anatomy. Further improvements could involve refining the database images' registration to target space using machine learning-based registration and incorporation of patient-specific data such as information on skull abnormalities provided by ZTE.

Conclusions

The presented approach for the CTR-AC method, based on a composite data base of multiple ^{68}Ge-transmission maps and structural MR images, provides accurately MRAC maps, and in contrast to most other published MRAC methods, even with continuous LAC values. CTR-AC shows a high accuracy, both in static and dynamic data, which is generally comparable to the best reported and commercially available MRAC methods so far. CTR-AC showed a near-zero bias in SUV and a similar low bias as found for ZTE-MRAC when using a kinetic modelling approach. This CTR-AC method is still experimental and not ready for routine application. However, the obtained results of this proof-of-concept study warrant further evaluations and methodological refinements in future work.

Funding

This work was supported by the Swedish Research Council, grant no. 2011–6269 and the Regional Medical Training and Research Agreement (Avtal om Läkarutbildning och Forskning, ALF) between Uppsala County and Uppsala University Hospital.

Availability of data and materials

João M. Sousa (joao.sousa@surgsci.uu.se) is the corresponding author for the data used in this manuscript.

Ethics approval and consent to participate

All procedures performed in studies involving human participants were in accordance with the ethical standards of the institutional and/or national research committee and with the 1964 Helsinki declaration and its later amendments or comparable ethical standards. Informed consent was obtained from all individual participants included in the study.

Declaration of Competing Interest

The authors declare the following financial interests/personal relationships which may be considered as potential competing interests: HA and ML receive research support and speaker fees from GE Healthcare.

Acknowledgments

The authors would like to express their gratitude to the staff of the PET centre, especially Anders Lundberg and Marie Åhlman at the PET/MR section, as well as the patients for their participation in the study.

Appendix A. Supplementary data

Supplementary data to this article can be found online at https://doi.org/10.1016/j.ejmp.2022.03.012.

References

[1] Schramm G, Langner J, Hofheinz F, Petr J, Beuthien-Baumann B, Platzek I, et al. Quantitative accuracy of attenuation correction in the Philips Ingenuity TF whole-body PET/MR system: a direct comparison with transmission-based attenuation correction. Magn Reson Mater Phys Biol Med 2013;26(1):115–26.

[2] Chen Y, An H. Attenuation correction of PET/MR imaging. Magn Reson Imaging Clin N Am 2017;25:245–55. https://doi.org/10.1016/j.mric.2016.12.001.

[3] Nakamoto Y, Osman M, Cohade C, Marshall LT, Links JM, Kohlmyer S, et al. PET/CT: comparison of quantitative tracer uptake between germanium and CT transmission attenuation-corrected images. J Nucl Med 2002;43:1137–43.

[4] Renner A, Rausch I, Cal Gonzalez J, Frass-Kriegl R, de Lara LN, Sieg J, et al. A head coil system with an integrated orbiting transmission point source mechanism for attenuation correction in PET/MRI. Phys Med Biol 2018;63. https://doi.org/10.1088/1361-6560/aae9a9.

[5] Teuho J, Torrado-Carvajal A, Herzog H, Anazodo U, Klén R, Iida H, et al. Magnetic resonance-based attenuation correction and scatter correction in neurological positron emission tomography/magnetic resonance imaging: current status with emerging applications. Front Phys 2020;7.

[6] Mecheter I, Alic L, Abbod M, Amira A, Ji J. MR image-based attenuation correction of brain PET imaging: review of literature on machine learning approaches for segmentation. J Digit Imaging 2020;33:1224–41. https://doi.org/10.1007/s10278-020-00361-x.

[7] Herzog H, Pietrzyk U, Shah NJ, Ziemons K. The current state, challenges and perspectives of MR-PET. Neuroimage 2010;49:2072–82. https://doi.org/10.1016/j.neuroimage.2009.10.036.

[8] Keereman V, Mollet P, Berker Y, Schulz V, Vandenberghe S. Challenges and current methods for attenuation correction in PET/MR. Magn Reson Mater Phys Biol Med 2013;26:81–98. https://doi.org/10.1007/s10334-012-0334-7.

[9] Barthel H, Schroeter ML, Hoffmann KT, Sabri O. PET/MR in dementia and other neurodegenerative diseases. Semin Nucl Med 2015;45:224–33. https://doi.org/10.1053/j.semnuclmed.2014.12.003.

[10] Chen Y, Juttukonda M, Su Yi, Benzinger T, Rubin BG, Lee YZ, et al. Probabilistic air segmentation and sparse regression estimated pseudo CT for PET/MR attenuation correction. Radiology 2015;275(2):562–9.

[11] Chen Z, Jamadar SD, Li S, Sforazzini F, Baran J, Ferris N, et al. From simultaneous to synergistic MR-PET brain imaging: A review of hybrid MR-PET imaging methodologies. Hum Brain Mapp 2018;39(12):5126–44.

[12] Ladefoged CN, Benoit D, Law I, Holm S, Kjær A, Højgaard L, et al. Region specific optimization of continuous linear attenuation coefficients based on UTE (RESOLUTE): Application to PET/MR brain imaging. Phys Med Biol 2015;60(20):8047–65.

[13] Delso G, Wiesinger F, Carl M, McKinnon G, Khalighi M, ter Voert E, et al. ZTE-based clinical bone imaging for PET/MR. J Nucl Med 2015;56:1806.

[14] Wiesinger F, Bylund M, Yang J, Kaushik S, Shanbhag D, Ahn S, et al. Zero TE-based pseudo-CT image conversion in the head and its application in PET/MR attenuation correction and MR-guided radiation therapy planning. Magn Reson Med 2018;80(4):1440–51.

[15] Sousa JM, Appel L, Engström M, Papadimitriou S, Nyholm D, Larsson E-M, et al. Evaluation of zero-echo-time attenuation correction for integrated PET/MR brain imaging—comparison to head atlas and 68Ge-transmission-based attenuation correction. EJNMMI Phys 2018;5(1). https://doi.org/10.1186/s40658-018-0220-0.

[16] Sousa JM, Appel L, Merida I, Heckemann RA, Costes N, Engström M, et al. Accuracy and precision of zero-echo-time, single- and multi-atlas attenuation correction for dynamic [11C]PE2I PET-MR brain imaging. EJNMMI Phys 2020;7(1). https://doi.org/10.1186/s40658-020-00347-2.

[17] Sekine T, ter Voert EEGW, Warnock G, Buck A, Huellner M, Veit-Haibach P, et al. Clinical evaluation of zero-echo-time attenuation correction for brain 18F-FDG PET/MRI: comparison with atlas attenuation correction. J Nucl Med 2016;57(12):1927–32.

[18] Wollenweber SD, Ambwani S, Delso G, Lonn AHR, Mullick R, Wiesinger F, et al. Evaluation of an atlas-based PET head attenuation correction using PET/CT & MR patient data. IEEE Trans Nucl Sci 2013;60:3383–90. https://doi.org/10.1109/TNS.2013.2273417.

[19] Mérida I, Reilhac A, Redouté J, Heckemann RA, Costes N, Hammers A. Multi-atlas attenuation correction supports full quantification of static and dynamic brain PET data in PET-MR. Phys Med Biol 2017;62:2834–58. https://doi.org/10.1088/1361-6560/aa5f6c.

[20] Burgos N, Cardoso MJ, Thielemans K, Modat M, Pedemonte S, Dickson J, et al. Attenuation correction synthesis for hybrid PET-MR scanners: Application to brain studies. IEEE Trans Med Imaging 2014;33(12):2332–41.

[21] Cabello J, Avram M, Brandl F, Mustafa M, Scherr M, Leucht C, et al. Impact of non-uniform attenuation correction in a dynamic [18F]-FDOPA brain PET/MRI study. EJNMMI Res 2019;9(1). https://doi.org/10.1186/s13550-019-0547-0.

[22] Kops ER, Herzog H, Shah NJ. Comparison template-based with CT-based attenuation correction for hybrid MR/PET scanners. EJNMMI Phys 2014;1:7364. https://doi.org/10.1186/2197-7364-1-s1-a47.

[23] Spuhler KD, Gardus J, Gao Yi, DeLorenzo C, Parsey R, Huang C. Synthesis of patient-specific transmission data for PET attenuation correction for PET/MRI neuroimaging using a convolutional neural network. J Nucl Med 2019;60(4):555–60.

[24] Ladefoged CN, Marner L, Hindsholm A, Law I, Højgaard L, Andersen FL. Deep learning based attenuation correction of PET/MRI in pediatric brain tumor patients: Evaluation in a clinical setting. Front Neurosci 2019;13:1–9. https://doi.org/10.3389/fnins.2018.01005.

[25] Liu F, Jang H, Kijowski R, Bradshaw T, McMillan AB. Deep Learning MR Imaging–based Attenuation Correction for PET/MR Imaging. Radiology 2018;286(2):676–84.

[26] Mehranian A, Zaidi H. Impact of time-of-flight PET on quantification errors in MR imaging-based attenuation correction. J Nucl Med 2015;56:635–41. https://doi.org/10.2967/jnumed.114.148817.

[27] Berker Y, Li Y. Attenuation correction in emission tomography using the emission data - A review. Med Phys 2016;43:807–32. https://doi.org/10.1118/1.4938264.

[28] Ladefoged CN, Law I, Anazodo U, St. Lawrence K, Izquierdo-Garcia D, Catana C, et al. A multi-centre evaluation of eleven clinically feasible brain PET/MRI attenuation correction techniques using a large cohort of patients. Neuroimage 2017;147:346–59.

[29] Rischka L, Gryglewski G, Berroterán-Infante N, Rausch I, James GM, Klöbl M, et al. Attenuation correction approaches for serotonin transporter quantification with PET/MRI. Front Physiol 2019;10. https://doi.org/10.3389/fphys.2019.01422.

[30] Schramm G, Koole M, Willekens SMA, Rezaei A, Van Weehaeghe D, Delso G, et al. Regional accuracy of ZTE-based attenuation correction in static [18F]FDG and dynamic [18F]PE2I brain PET/MR. Front Phys 2019;7. https://doi.org/10.3389/fphy.2019.00211.

[31] Rota Kops E, Hautzel H, Herzog H, Antoch G, Shah NJ. Comparison of template-based versus CT-based attenuation correction for hybrid MR/PET scanners. IEEE Trans Nucl Sci 2015;62:2115–21. https://doi.org/10.1109/TNS.2015.2452574.

[32] Jenkinson M, Smith S. A global optimisation method for robust affine registration of brain images. Med Image Anal 2001;5(2):143–56.

[33] Jenkinson M, Bannister P, Brady M, Smith S. Improved optimization for the robust and accurate linear registration and motion correction of brain images. Neuroimage 2002;17:825–41. https://doi.org/10.1006/nimg.2002.1132.

[34] Penny W, Friston K, Ashburner J, Kiebel S, Nichols T. Statistical Parametric Mapping: The Analysis of Functional Brain Images. 1st ed. Academic Press; 2007. 10.1016/B978-0-12-372560-8.X5000-1.

[35] Svarer C, Madsen K, Hasselbalch SG, Pinborg LH, Haugbøl S, Frøkjær VG, et al. MR-based automatic delineation of volumes of interest in human brain PET images using probability maps. Neuroimage 2005;24(4):969–79.

[36] Gunn RN, Lammertsma AA, Hume SP, Cunningham VJ. Parametric imaging of ligand-receptor binding in PET using a simplified reference region model. Neuroimage 1997;6:279–87. https://doi.org/10.1006/nimg.1997.0303.

[37] Lammertsma AA, Hume SP. Simplified reference tissue model for PET receptor studies. Neuroimage 1996;4:153–8. https://doi.org/10.1006/nimg.1996.0066.

[38] Appel L, Jonasson My, Danfors T, Nyholm D, Askmark H, Lubberink M, et al. Use of 11C-PE2I PET in differential diagnosis of Parkinsonian disorders. J Nucl Med 2015;56(2):234–42.

[39] Wiesinger F, Sacolick LI, Menini A, Kaushik SS, Ahn S, Veit-Haibach P, et al. Zero TE MR bone imaging in the head. Magn Reson Med 2016;75(1):107–14.

[40] Gong K, Yang J, Kim K, El Fakhri G, Seo Y, Li Q. Attenuation correction for brain PET imaging using deep neural network based on Dixon and ZTE MR images. Phys Med Biol 2018;63(12):125011.

[41] Blanc-Durand P, Khalife M, Sgard B, Kaushik S, Soret M, Tiss A, et al. Attenuation correction using 3D deep convolutional neural network for brain 18F-FDG PET/MR: Comparison with Atlas, ZTE and CT based attenuation correction. PLoS ONE 2019;14(10):e0223141.

[42] Mannheim JG, Cheng J-C, Vafai N, Shahinfard E, English C, McKenzie J, et al. Cross-validation study between the HRRT and the PET component of the SIGNA PET/MRI system with focus on neuroimaging. EJNMMI Phys 2021;8(1). https://doi.org/10.1186/s40658-020-00349-0.